BATTERIES

Kinetic pathways of ionic transport in fast-charging lithium titanate

Wei Zhang[1]*†, Dong-Hwa Seo[2]*‡, Tina Chen[2,3]*, Lijun Wu[4], Mehmet Topsakal[5], Yimei Zhu[4], Deyu Lu[5], Gerbrand Ceder[2,3]§, Feng Wang[1]§

Fast-charging batteries typically use electrodes capable of accommodating lithium continuously by means of solid-solution transformation because they have few kinetic barriers apart from ionic diffusion. One exception is lithium titanate ($Li_4Ti_5O_{12}$), an anode exhibiting extraordinary rate capability apparently inconsistent with its two-phase reaction and slow Li diffusion in both phases. Through real-time tracking of Li^+ migration using operando electron energy-loss spectroscopy, we reveal that facile transport in $Li_{4+x}Ti_5O_{12}$ is enabled by kinetic pathways comprising distorted Li polyhedra in metastable intermediates along two-phase boundaries. Our work demonstrates that high-rate capability may be enabled by accessing the energy landscape above the ground state, which may have fundamentally different kinetic mechanisms from the ground-state macroscopic phases. This insight should present new opportunities in searching for high-rate electrode materials.

Ionic transport in solids provides the basis of operation for electrochemical energy conversion and storage devices, such as lithium (Li)–ion batteries (LIBs), which function by storing and releasing Li^+ ions in electrode materials. During these processes, Li^+-ion transport is often coupled with phase transformations in the operating electrodes (*1*, *2*). For fast-charging applications, electrode materials capable of accommodating Li continuously through solid-solution transformation are preferentially used because they have few kinetic barriers apart from Li^+-ion diffusion in the solid state (*3*, *4*). An exception is lithium titanate (LTO), an appealing anode capable of fast charging without the issue of Li plating identified in graphite (*5*). LTO accommodates Li through a two-phase process, during which the initial disordered spinel phase ($Li_4Ti_5O_{12}$; space group $Fd\bar{3}m$) transforms directly into a rock-salt phase ($Li_7Ti_5O_{12}$; $Fm\bar{3}m$) with negligible volume change (i.e., zero strain) (*6*–*8*). Microscopically, Li insertion into the octahedral 16c sites is accompanied by Li^+-ion migration from the tetrahedral 8a to the 16c sites. However, because Li^+-ion mobility is poor in the end-members ($Li_4Ti_5O_{12}$ and $Li_7Ti_5O_{12}$), a model in which these two phases coexist macroscopically conflicts with the high Li^+ -ion mobility observed at intermediate concentrations (*9*–*11*).

This puzzling behavior has recently been attributed to the existence of an intermediate state ($Li_{4+x}Ti_5O_{12}$; $0 \le x \le 3$) with Li^+ ions simultaneously occupying face-sharing 8a and 16c sites, in the form of either a homogenous solid solution or a mixture of phase-separated nanometer-sized domains (*10*, *12*). In situ x-ray absorption spectroscopy studies provided evidence of the metastable $Li_{4+x}Ti_5O_{12}$ state, which emerges upon Li insertion even at low rates (*13*). Computational studies have predicted that face-sharing 8a and 16c local motifs are stabilized at the $Li_4Ti_5O_{12}/Li_7Ti_5O_{12}$ phase boundaries owing to the presence of Li occupying the 16d sites (*12*). However, because of the nonequilibrium nature of the ionic transport (*12*, *13*), the kinetic pathways and underlying mechanisms enabling facile ionic transport in LTO remain unresolved.

With available characterization techniques, it has been challenging to determine the atomic configuration of the metastable intermediates ($Li_{4+x}Ti_5O_{12}$) and the associated Li^+-ion transport pathways (*6*, *13*, *14*). Li K-edge electron energy-loss spectroscopy (Li-EELS), more specifically the energy-loss near-edge structure, shows promise for probing the site occupancy of Li in lithiated electrodes because of its high sensitivity to the local environment surrounding Li (*15*). Compared with other Li-sensitive techniques, such as nuclear magnetic resonance (NMR) spectroscopy (*10*) and neutron diffraction (*16*), EELS in the transmission electron microscope (TEM) has the intrinsic advantages of high spatial and temporal resolution (*17*). However, because the low-lying Li K edge (~60 eV) is in immediate proximity to the strong plasmon excitations, plural inelastic scattering may arise in the presence of thick membranes and liquid electrolyte in electrochemical cells, complicating operando Li-EELS measurements (*18*).

We developed an ionic liquid electrolyte (ILE)–based electrochemical cell for operation inside a TEM, with a configuration resembling that of a real battery, enabling operando Li-EELS probing of Li occupancy and transport in LTO upon galvanostatic (dis)charging at varying rates. Through combined operando Li-EELS and first-principles studies, we identified representative metastable $Li_{4+x}Ti_5O_{12}$ configurations, consisting of distorted Li polyhedra at the reaction front, which provide distinct Li^+-ion migration pathways with substantially lower activation energy than those in the end-members and which dominate the kinetics of Li^+-ion transport in LTO.

Figure 1A shows the design of the electrochemical cell for operando Li-EELS measurements, adapted from a TEM grid–based cell (*19*). The cell uses ILE containing 1.0 M lithium bis (trifluoromethanesulfonyl)imide in 1-butyl-1-methylpyrrolidinium bis(trifluoromethylsulfonyl) imide, a nonflammable electrolyte that has been increasingly used for batteries (*20*). Because of its low vapor pressure, ILE is compatible with the high-vacuum environment in the TEM column, thereby avoiding the thick membranes generally required in liquid cells. By controlling the ILE thickness (to 10 nm or less) and collection angle (below 1.0 mrad), plural plasmon excitation was largely suppressed (fig. S1), enabling the collection of high-quality, low-energy lying Li-EELS spectra (*21*). The electrochemical functionality of the cell was tested by galvanostatic cycling of LTO electrodes, with rates spanning from 0.8 to 8 C [see the method of estimating C-rate in the Operando TEM-EELS experiments of (*22*)]. The electrochemical performance, with flat voltage plateaus at ~1.55 V and sharp redox peaks in the cyclic voltammetry curves (Fig. 1B and fig. S2), is comparable to that in regular LIB cells. Such an ILE-based electrochemical cell was used in operando Li-EELS experiments to track Li^+-ion migration in LTO nanoparticles with well-defined structure and morphology (fig. S3). Li-EELS in the pre-edge region provides key information about the occupancy and migration of Li^+ ions among different sites (e.g., 8a in $Li_4Ti_5O_{12}$, 16c in $Li_7Ti_5O_{12}$, and other polyhedral sites associated with $Li_{4+x}Ti_5O_{12}$), as illustrated in Fig. 1C.

Figure 2 presents the time-resolved Li-EELS spectra obtained from a few selected nanoparticles (Fig. 2A and fig. S4) during the first cycle at a rate equivalent to 2 C. EELS spectra of the Ti L- and O K-edges were also obtained before and after (dis)charge (fig. S5), confirming active Ti redox [section 2 in (*22*)]. As shown in Fig. 2C, the main peak in the Li-EELS spectra remained at the same energy position

[1]Sustainable Energy Technologies Department, Brookhaven National Laboratory, Upton, NY 11973, USA. [2]Department of Materials Science and Engineering, University of California, Berkeley, Berkeley, CA 94720, USA. [3]Materials Sciences Division, Lawrence Berkeley National Laboratory, Berkeley, CA 94720, USA [4]Department of Condensed Matter Physics and Materials Science, Brookhaven National Laboratory, Upton, NY 11973, USA. [5]Center for Functional Nanomaterials, Brookhaven National Laboratory, Upton, NY 11973, USA. *These authors contributed equally to this work. †Present address: Key Laboratory of Advanced Energy Materials Chemistry (Ministry of Education), College of Chemistry, Nankai University, Tianjin 300071, P. R. China. ‡Present address: Department of Energy Engineering, School of Energy and Chemical Engineering, Ulsan National Institute of Science and Technology (UNIST), Ulsan 44919, Republic of Korea. §Corresponding author. Email: gceder@berkeley.edu (G.C.); fwang@bnl.gov (F.W.)

(~61.5 eV) during cycling. Nonetheless, subtle but clear changes occurred within the pre-edge region, as shown in the intensity map of the spectra in Fig. 2, C and D. In the spectrum of $Li_4Ti_5O_{12}$, a broad peak in the pre-edge region (called pre-peak hereafter) appeared at ~58.9 eV (labeled by "S") (see also fig. S6), which mainly comes from the inelastic scattering of $Li_{(8a)}$ sites (*15*). The pre-peak from $Li_{(16c)}$ sites in $Li_7Ti_5O_{12}$ appears at the same energy, despite the different local Li environment in the two end-members (fig. S6).

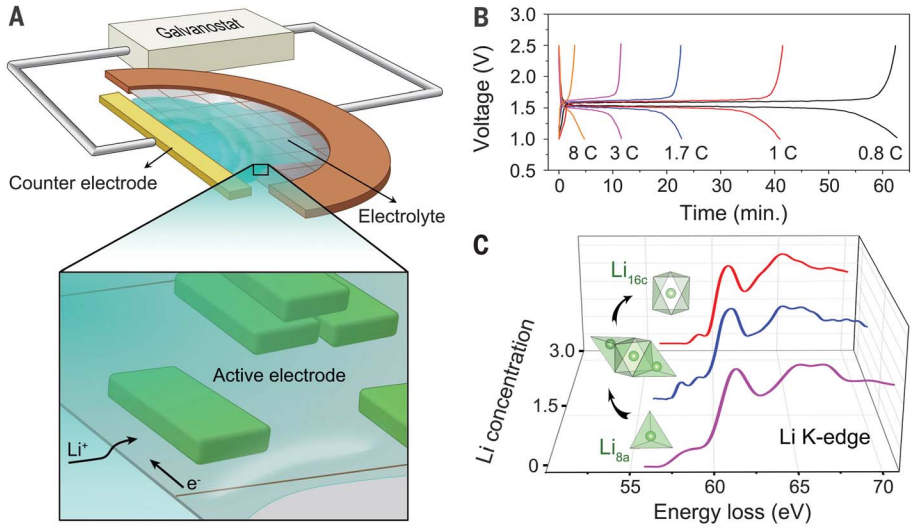

Fig. 1. Design of an electrochemically functional cell for operando characterization of battery materials inside a TEM. (**A**) Schematic of the ILE-based electrochemical cell, with a configuration similar to that of regular batteries with the active electrode (e.g., LTO nanoparticles marked by green color; inset) loaded on a carbon film (gray) as a working electrode, matched with Li metal (yellow) immersed in ILE (light green). (**B**) Voltage profiles of LTO nanoparticles in the ILE-based electrochemical cell during galvanostatic discharge and charge at different rates (fig. S2 shows comparison with cycling tests in regular coin-type cells). (**C**) Representative Li-EELS spectra obtained from LTO nanoparticles at different lithiated states, revealing the migration of Li^+ ions from the initial tetrahedral 8a sites in $Li_4Ti_5O_{12}$ to polyhedral sites in an intermediate to the final octahedral 16c sites in $Li_7Ti_5O_{12}$ (as illustrated in the inset).

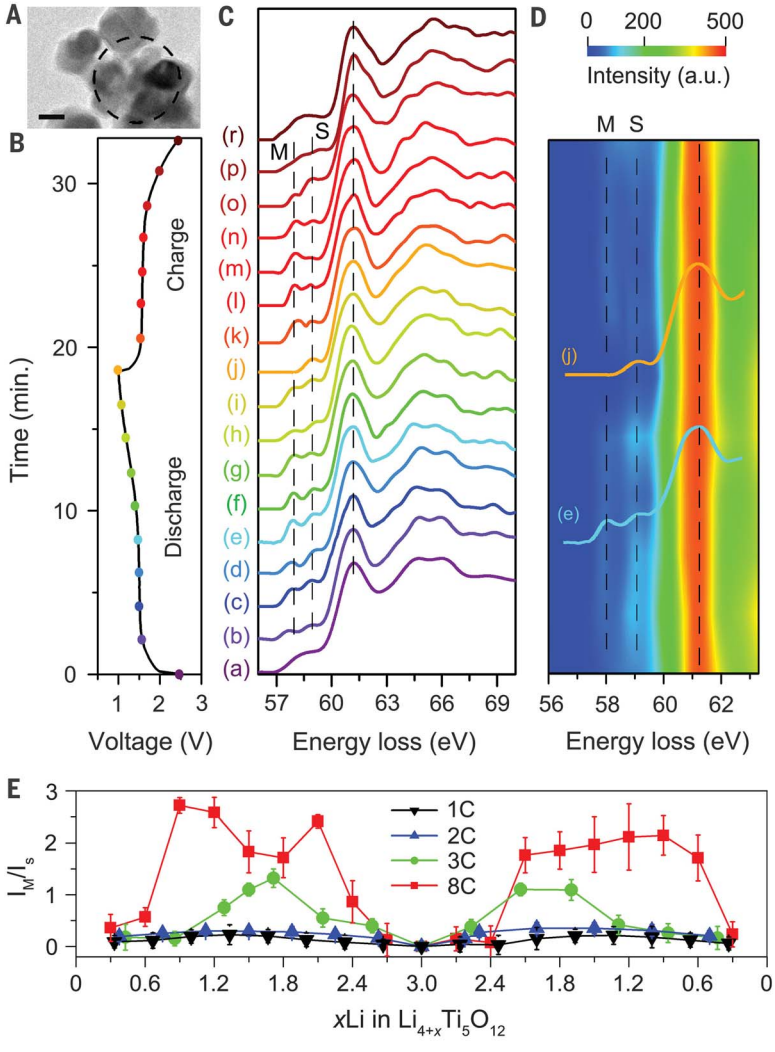

Fig. 2. Real-time probing of Li^+-ion transport in LTO during discharge and charge using operando Li-EELS. (**A**) Bright-field TEM image showing the LTO nanoparticles selected for obtaining Li-EELS spectra (marked by a black dashed circle). Scale bar, 50 nm. (**B** and **C**) Voltage profiles of LTO nanoparticles and the corresponding EELS spectra selected with an interval of 120 s during the first cycle at 2 C rate [marked by color-coded dots in (B) and letters in (C)]. The vertical dashed black lines indicate the energy positions of the main peaks at ~61.5 eV and pre-peaks M (related to metastable configurations of the intermediate compositions) and S (related to stable configurations in $Li_4Ti_5O_{12}$ and $Li_7Ti_5O_{12}$). (**D**) Intensity map of the Li-EELS spectra at a 2 C rate (fig. S8 shows EELS spectra and intensity maps at 1 C, 3 C, and 8 C rates). Two representative spectra (e) and (j) are displayed to show the pre-edge features, M and S. a.u., arbitrary units. (**E**) Intensity ratio of the two pre-peaks, M and S (I_M/I_S) as a function of Li concentration (x) at different rates (1 C, 2 C, 3 C, and 8 C), in which I_M and I_S are the integrated intensities of pre-peaks M and S, respectively.

Upon discharging and subsequent charging, the pre-peak S remained at nearly the same position. However, a new pre-peak emerged at ~58.0 eV (labeled by "M"), which is absent in the spectra of the two end-members (Fig. 2D) as well as the partially lithiated LTO electrodes in ex situ measurements [section 3 in (*22*)] (fig. S7). Pre-peak M was commonly observed across the electrode, and its intensity was found to be strongly rate-dependent (fig. S8). The ratio of integrated intensity of the two pre-peaks M and S (defined as I_M/I_S) as a function of Li concentration (x) was plotted in Fig. 2E. At low rates (1 C and 2 C), I_M/I_S values are small (only ~0.2) but increase abruptly (to ~2.0) at high rates (3 C and 8 C) [quantitative analysis in section 4 of (*22*)]. As shown below, the evolution of features in the Li-EELS spectra (e.g., I_M/I_S ratio) provides key information about Li occupancy and migration in the metastable intermediates ($Li_{4+x}Ti_5O_{12}$) and its rate-dependent behaviors.

To understand the origin of the pre-edge features in the Li-EELS spectra and their evolution during charge and discharge, we studied the local configurations of Li^+ ions in the two end-members ($Li_4Ti_5O_{12}$ and $Li_7Ti_5O_{12}$) and the intermediates ($Li_{4+x}Ti_5O_{12}$, x = 1 and 2) using density functional theory (DFT) (*22*). In the low-energy structures of $Li_{4+x}Ti_5O_{12}$, one of the $Li_{(8a)}$ tetrahedra shares a three-coordinated oxygen face with a $Li_{(16c)}$ octahedron at the domain boundary between $Li_4Ti_5O_{12}$ and $Li_7Ti_5O_{12}$ (fig. S9, C and D). The face-sharing $Li_{(8a)}$ and $Li_{(16c)}$ polyhedra are highly distorted compared to the unperturbed $Li_{(8a)}$ and $Li_{(16c)}$ polyhedra in $Li_4Ti_5O_{12}$ and $Li_7Ti_5O_{12}$ and are stabilized by neighboring $Li_{(16d)}$ octahedra [section 5 in (*22*)], which is consistent with recent DFT calculations (*12*). Within 100 meV/O_4, a large number of relevant atomic configurations exist with different local environments, especially local motifs of $Li_{(8a)}$-$Li_{(16c)}$ face-sharing polyhedra with various levels of distortion (fig. S10). The DFT-based sampling of the $Li_{4+x}Ti_5O_{12}$ potential landscape reveals that a very large configuration space can be accessed, even within the formation energy of 100 meV/O_4 [the nature of these intermediate configurations is described further in sections 5 and 8 in (*22*)].

After establishing the structural models of $Li_{4+x}Ti_5O_{12}$ at different Li concentrations (x = 0, 1, 2, and 3), we calculated the corresponding Li-EELS spectra for Li at the 8a, 16c, and 16d sites for the most stable configurations of $Li_{4+x}Ti_5O_{12}$ using the Z + 1 approach (where Z refers to the atomic number) to model the core-hole effect [computational details in (*22*)]. Because the pre-edge peaks originate predominantly from the intra-atomic Li 1s to 2p transition, this level of description is adequate. The good agreement in the near-edge region of the end-members between the Z + 1 method and the Bethe-Salpeter equation–based method supports our choice of method (fig. S11). The energy positions of pre-peak S in the computed spectra and their relative intensities compared with those of the main peak for both $Li_4Ti_5O_{12}$ and $Li_7Ti_5O_{12}$ are in good agreement with the experimental results (fig. S12A), validating the Z + 1 method used for computing the Li-EELS spectra. The Li-EELS spectra of $Li_{(8a)}$ in the most stable $Li_5Ti_5O_{12}$ and $Li_6Ti_5O_{12}$ configurations are almost the same as those of $Li_{(8a)}$ in $Li_4Ti_5O_{12}$, especially near the pre-peak region (Fig. 3A). However, a new pre-peak appears at ~58 eV in the EELS spectra of face-sharing $Li_{(16c)}$ that is absent in the computed spectra of $Li_{(16c)}$ in $Li_7Ti_5O_{12}$ and $Li_{(16d)}$ at any composition (Fig. 3B; fig. S12, B and C; and fig. S14). Because this new pre-peak coincides in energy with pre-peak M observed in the operando EELS measurements (Fig. 2B), we assign pre-peak M in the Li-EELS spectra at low rates to the inelastic scattering from distorted face-sharing $Li_{(16c)}$ in the metastable configurations. Owing to the distortion of face-sharing $Li_{(16c)}$, several Li–O bonds are elongated, which breaks the degeneracy of Li–O coupling. A representative configuration is shown in Fig. 3C that demonstrates elongated Li–O bond lengths of 2.33 to 2.50 Å in $Li_5Ti_5O_{12}$, considerably longer than those in $Li_7Ti_5O_{12}$ (2.06 to 2.20 Å). The weakened Li–O bonds effectively pull the antibonding Li–O states to lower energy and cause the pre-peak to split, giving rise to pre-peak M in the EELS spectra. The corresponding partial charge densities are shown in the isosurface plot in Fig. 3C. Whereas the partial charge density associated with pre-peak M concentrates more heavily on O atoms with longer Li–O bonds, the partial charge density of pre-peak S is distributed evenly on all O atoms regardless of Li–O bond

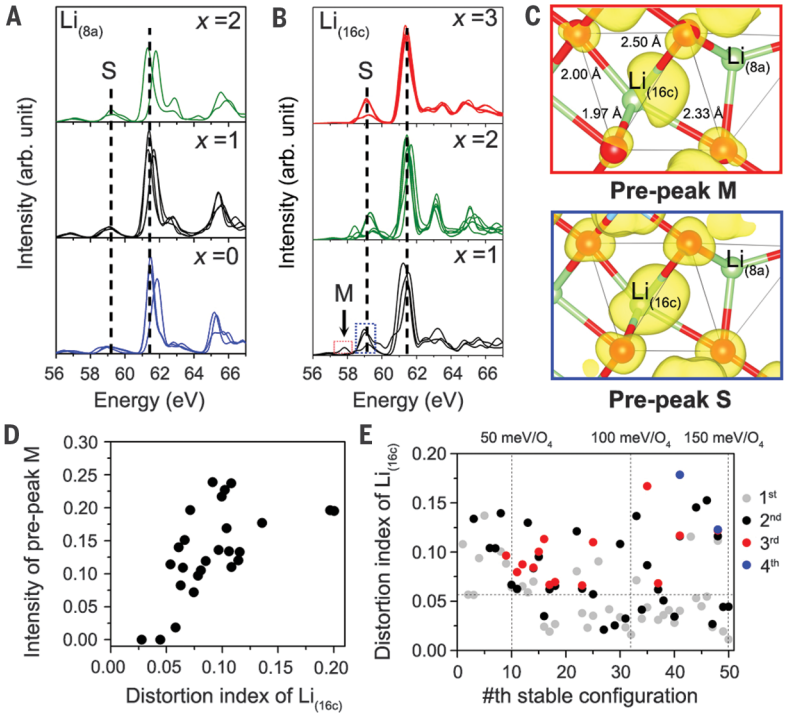

Fig. 3. Identification of Li-EELS fingerprints for Li-polyhedral configurations in $Li_{4+x}Ti_5O_{12}$ (0 ≤ x ≤ 3) by DFT calculations. (**A** and **B**) Calculated Li-EELS spectra of $Li_{4+x}Ti_5O_{12}$ (x = 0, 1, and 2) for Li at 8a sites and $Li_{4+x}Ti_5O_{12}$ (x = 1, 2 and 3) for Li at 16c sites, respectively. The dashed lines in (A) and (B) mark the energy positions of the main peaks and pre-peak S. The black arrow in (B) indicates the pre-peak M from face-sharing $Li_{(16c)}$ in $Li_5Ti_5O_{12}$ and $Li_6Ti_5O_{12}$, which is not observed for $Li_{(16c)}$ in $Li_7Ti_5O_{12}$. arb. unit, arbitrary unit. (**C**) Isosurface of partial charge density around face-sharing $Li_{(16c)}$ in $Li_5Ti_5O_{12}$ in the energy range of pre-peak M and pre-peak S, as marked with dashed red and blue boxes, respectively, in (B), with 0.015 of isovalue. Bond lengths between $Li_{(16c)}$ and O ions are labeled. (**D**) Intensity of the pre-peak M as a function of distortion index (d) of face-sharing $Li_{(16c)}$ for various Li configurations in $Li_5Ti_5O_{12}$ and $Li_6Ti_5O_{12}$. (**E**) d of face-sharing $Li_{(16c)}$ in the nth stable configuration (ordered by formation energy) of $Li_5Ti_5O_{12}$. The horizontal and vertical dashed lines indicate the approximate value of d above which pre-peak M appears and the formation energy of the nth stable configuration at 50, 100, and 150 meV/O_4. When a single configuration contains multiple face-sharing $Li_{(16c)}$, the different face-sharing $Li_{(16c)}$ are labeled as colored points according to their d values in the ascending order: gray (first lowest distortion index), black (second), red (third), and blue (fourth).

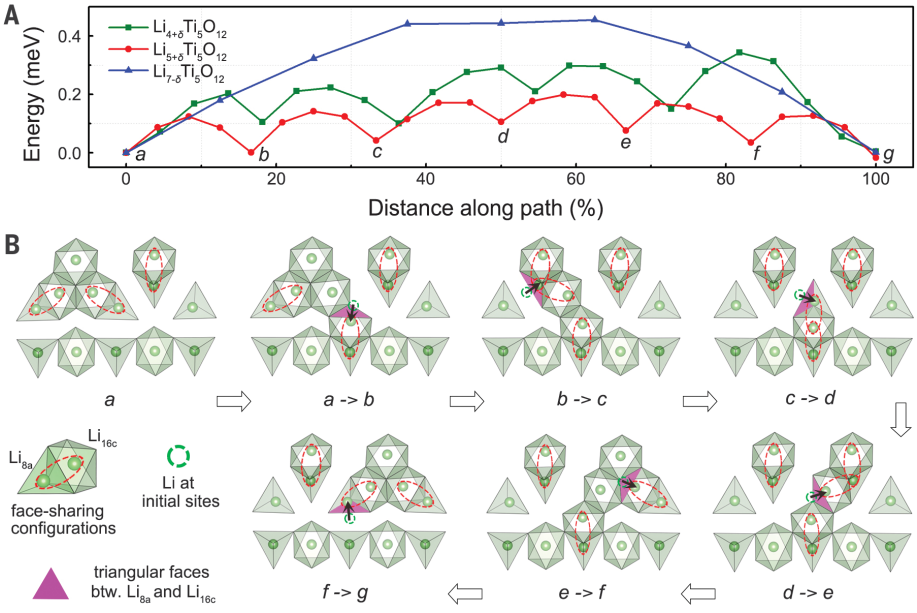

Fig. 4. Li^+-ion migration pathways and the corresponding energy barriers in the intermediates. (**A**) Energy profile of the pathways in $Li_{4+\delta}Ti_5O_{12}$ (green), $Li_{5+\delta}Ti_5O_{12}$ (red), and $Li_{7-\delta}Ti_5O_{12}$ (blue) as a function of distance along the paths. (**B**) Migration pathways involved for each step, from a to g, in one representative intermediate, $Li_{5+\delta}Ti_5O_{12}$ (movie S1 shows the trajectories of Li^+-ion migration in $Li_{5+\delta}Ti_5O_{12}$). The translucent green spots mark the initial Li sites during each substep of migration. The black arrows indicate the migration direction of each substep. The three-coordinated oxygen face through which the Li^+ ions migrate from a Li_{8a} tetrahedron to a Li_{16c} octahedron is colored purple. The Li^+-ion migration pathways in $Li_{4+\delta}Ti_5O_{12}$ and $Li_{7-\delta}Ti_5O_{12}$ are provided in movie S2 and figs. S23 and S24. btw., between.

lengths (see also the projected density of states in fig. S13).

To understand the effect of high (dis)charge rate on pre-peak M in the Li-EELS spectra (Fig. 2E), we also computed the Li-EELS spectra of $Li_5Ti_5O_{12}$ and $Li_6Ti_5O_{12}$ configurations with higher formation energies (which are accessible at higher current rates or large overpotential) . Figure S10 shows that the distortion of face-sharing $Li_{(16c)}$ and $Li_{(8a)}$ polyhedra is affected by the presence of neighboring $Li_{(16d)}$ or $Ti_{(16d)}$ (*22*). The varying local environment results in different intensities and energy levels of pre-peak M [section 7 in (*22*)]. Face-sharing $Li_{(16c)}$ and $Li_{(8a)}$ polyhedra in various $Li_{4+x}Ti_5O_{12}$ with distortion index [*d*; eq. S2 in (*22*)] larger than ~0.06 result in the appearance of pre-peak M, whose intensity tends to increase with *d* [Fig. 3D, fig. S17, and section 7 in (*22*)]. Such high distortion levels reduce the effective coordination number of $Li_{(16c)}$ and $Li_{(8a)}$. On the basis of the coordination number weighting scheme of (*23*), $Li_{(16c)}$ and $Li_{(8a)}$ with $d \sim 0.06$ are found to be undercoordinated with effective coordination numbers of 4.7 and 3.6 (fig. S18), respectively, rather than the expected 6 and 4. Similar trends showing a more pronounced pre-peak with undercoordinated local environments are well established in transition-metal K-edge x-ray absorption near-edge structures (*24*). As observed in Fig. 3E and fig. S19, highly distorted face-sharing $Li_{(16c)}$ and $Li_{(8a)}$ polyhedra with *d* higher than 0.06 appear more frequently as the formation energy of the intermediate $Li_5Ti_5O_{12}$ and $Li_6Ti_5O_{12}$ increases. This is consistent with the presence of more face-sharing $Li_{(16c)}$ and $Li_{(8a)}$ polyhedra in $Li_5Ti_5O_{12}$ configurations with higher formation energies, as indicated by the points with different colors in Fig. 3E. Highly distorted face-sharing $Li_{(8a)}$ tetrahedra are observed much less often than highly distorted $Li_{(16c)}$ octahedra in configurations with formation energy less than 100 meV/O_4 (Fig. 3E and fig. S19). Therefore, the appearance of pre-peak M is mainly attributed to face-sharing $Li_{(16c)}$ octahedra at low current rates but to both face-sharing $Li_{(16c)}$ and $Li_{(8a)}$ polyhedra at high current rates.

Phase transformation through a solid-solution path is favorable for high-rate performance in many electrodes, such as $LiFePO_4$ (LFP) (*3*, *4*). However, LTO undergoes a first-order phase transition (*6*, *12*) because the macroscopic solid solution is largely inaccessible owing to its high formation energy, in contrast to the low formation energies of the metastable solid solution in LFP [sections 5 and 8 in (*22*)]. Instead, (de)lithiation proceeds by means of a two-phase reaction, involving face-sharing $Li_{(8a)}$–$Li_{(16c)}$ local motifs at the boundaries between the phase domains (*12*, *13*), which are nanosized because of the low formation energy of the interfaces [section 8 in (*22*)]. Hence, whereas the origin of the fast rate in LFP is the low energy of the metastable solid solution, it is the low interfacial energy in LTO that creates nanosized domains of each phase and provides the interfacial pathways for fast Li^+-ion transport. Our results are generally consistent with the two-phase model (*12*, *13*), as we observed mainly interfacial-type configurations at lower energy [sections 5 and 8 in (*22*)]. However, our results further reveal a large variety of face-sharing $Li_{(8a)}$–$Li_{(16c)}$ local motifs in the intermediate $Li_{4+x}Ti_5O_{12}$ configurations. These local motifs, whose number and distortion index display rate dependence, may affect the kinetics in intermediate compositions.

To obtain a mechanistic understanding of fast Li diffusion in LTO, we performed nudged–elastic-band (*25*, *26*) calculations that account for distorted face-sharing Li polyhedra (Fig. 4 and figs. S23 and S24). The activation energies of Li^+-ion migration in the lowest-energy $Li_4Ti_5O_{12}$ and $Li_5Ti_5O_{12}$ (with an interstitial Li^+) and $Li_7Ti_5O_{12}$ (with a vacancy) configurations are ~343, ~216, and ~455 meV, respectively (Fig. 4A). The low activation energy of $Li_5Ti_5O_{12}$ is in line with the low migration barriers previously obtained from NMR measurements (*10*) and ab initio molecular dynamics (*12*). Our results indicate that facile Li^+ migration occurs at the two-phase boundaries containing face-sharing Li polyhedra, which is associated with lower activation barriers compared with those in the end-members. In general, the Li^+-ion diffusion pathway involves Li hopping from face-sharing tetrahedral (octahedral) Li sites to octahedral (tetrahedral) Li sites (Fig. 4B and fig. S23, B to H). Along this path, although face-sharing Li^+ ions change position, the number of face-sharing Li^+ ions (three to four) remains nearly constant in the $Li_4Ti_5O_{12}$ (always two) and $Li_5Ti_5O_{12}$ (from three to four to three) pathways. As a result, there is no abrupt increase of the energy of the system. In the higher-energy pathway in $Li_7Ti_5O_{12}$, however, the number of face-sharing Li^+-ions changes substantially from zero to two and back to zero (fig. S24, B to D). The low migration barrier for Li^+ ions in the LTO system can be attributed to two important factors: (i) The number of face-sharing Li polyhedra is smaller in the transition state (when the migrating Li^+ ions are in the triangular face in Fig. 4B) than in the initial and final states within each step [for example, there are three instances of face-sharing in states *a* and *b* (marked in Fig. 4) but only two between *a* and *b* in Fig. 4B]. The reduction in Li^+ – Li^+ repulsion in the transition state is likely to lower the activation barrier. (ii) Because local distortion helps to reduce the effective coordination number of Li (fig. S18), the change in Li coordination is minimized

during Li^+-ion migration through the three-coordinated oxygen face, further lowering the activation barrier (*27*). Both factors minimize changes in the energy, resulting in a relatively flat energy landscape along the migration path, as described in Fig. 4A. Our analysis implies that the improved kinetics at higher rate results from the increased amount of face-sharing Li^+, and thus mobile carriers, and the more highly distorted Li polyhedra seen in the high-energy $Li_{4+x}Ti_5O_{12}$ configurations accessible at high rates.

In this study, we developed an electrochemically functional cell operating inside a TEM that allows operando characterization of electrode materials under real electrochemical conditions. Facile Li^+-ion migration routes were revealed in intermediate configurations involving face-sharing Li polyhedra. The associated low Li^+-ion migration barriers of the face-sharing motifs along with the low formation energy of the interfaces reconcile the apparent contradiction between the high-rate capability of LTO and the poor Li^+-ion conductivity of its end-member phases. Findings from this study, particularly on the improved kinetics originating from the face-sharing Li motifs in intermediate configurations that become accessible at high rates, provide insights into designing electrode materials for fast-charging batteries.

REFERENCES AND NOTES

1. J. Maier, *Nat. Mater.* **4**, 805–815 (2005).
2. C. Zhu, R. E. Usiskin, Y. Yu, J. Maier, *Science* **358**, eaao2808 (2017).
3. H. Liu *et al*., *Science* **344**, 1252817 (2014).
4. R. Malik, F. Zhou, G. Ceder, *Nat. Mater.* **10**, 587–590 (2011).
5. T.-F. Yi, S.-Y. Yang, Y. Xie, *J. Mater. Chem. A Mater. Energy Sustain.* **3**, 5750–5777 (2015).
6. S. Scharner, W. Weppner, P. Schmid-Beurmann, *J. Electrochem. Soc.* **146**, 857–861 (1999).
7. M. Wagemaker *et al*., *Adv. Mater.* **18**, 3169–3173 (2006).
8. B. Ziebarth, M. Klinsmann, T. Eckl, C. Elsässer, *Phys. Rev. B Condens. Matter Mater. Phys.* **89**, 174301 (2014).
9. H. Hain *et al*., *Solid State Nucl. Magn. Reson.* **42**, 9–16 (2012).
10. W. Schmidt *et al*., *Chem. Mater.* **27**, 1740–1750 (2015).
11. M. Wilkening *et al*., *Phys. Chem. Chem. Phys.* **9**, 6199–6202 (2007).
12. S. Ganapathy, A. Vasileiadis, J. R. Heringa, M. Wagemaker, *Adv. Energy Mater.* **7**, 1601781 (2017).
13. W. Zhang *et al*., *J. Am. Chem. Soc.* **139**, 16591–16603 (2017).
14. C. P. Grey, J. M. Tarascon, *Nat. Mater.* **16**, 45–56 (2016).
15. F. Wang *et al*., *Nanotechnology* **24**, 424006 (2013).
16. O. Dolotko *et al*., *Solid State Sci.* **36**, 101–106 (2014).
17. R. F. Egerton, *Electron Energy-Loss Spectroscopy in the Electron Microscope* (Springer Science & Business Media, 2011).
18. F. M. Ross, *Science* **350**, aaa9886 (2015).
19. F. Wang *et al*., *Nat. Commun.* **3**, 1201 (2012).
20. M. Armand, F. Endres, D. R. MacFarlane, H. Ohno, B. Scrosati, *Nat. Mater.* **8**, 621–629 (2009).
21. F. Wang *et al*., *ACS Nano* **5**, 1190–1197 (2011).
22. Supplementary materials.
23. K. Robinson, G. V. Gibbs, P. H. Ribbe, *Science* **172**, 567–570 (1971).
24. T. Yamamoto, *XRay Spectrom.* **37**, 572–584 (2008).
25. G. Henkelman, H. Jónsson, *J. Chem. Phys.* **113**, 9978–9985 (2000).
26. D. Sheppard, R. Terrell, G. Henkelman, *J. Chem. Phys.* **128**, 134106 (2008).
27. Z. Rong *et al*., *Chem. Mater.* **27**, 6016–6021 (2015).

ACKNOWLEDGMENTS

We thank H. Zhao, X. Hu, and Y. Celebi for help with electrode fabrication and discussion on data interpretation. We thank T. Bowman for the graphic design (Fig. 1A). **Funding:** This work was partially supported by the Laboratory Directed Research and Development program at the Brookhaven National Lab (BNL) (contract no. DE-SC0012704). This research used resources of the Center for Functional Nanomaterials, which is a U.S. Department of Energy (DOE) Office of Science facility, and the Scientific Data and Computing Center, a component of the BNL Computational Science Initiative, at BNL (contract no. DE-SC0012704). This work was supported in part by the Assistant Secretary for Energy Efficiency and Renewable Energy, Vehicle Technologies Office, of the U.S. DOE (contract no. DE-AC02-05CH11231), under the Advanced Battery Materials Research (BMR) Program and by the National Science Foundation Graduate Research Fellowship (grant no. DGE 1106400). Efforts by F.W. involving writing and revision of the manuscript were supported by U.S. DOE, Office of Energy Efficiency and Renewable Energy, Vehicle Technologies Office (contract no. DE-SC0012704). Efforts on EELS data analysis by L.W. and Y.Z. were supported by the U.S. DOE, Office of Basic Energy Science, Division of Materials Science and Engineering (contract no. DE-SC0012704). T.C. thanks the National Science Foundation's Extreme Science and Engineering Development Environment (XSEDE) supercomputer Stampede2 (allocation TG-DMR970008S), which is supported by the National Science Foundation (grant no. ACI-1548562), for providing computing resources. **Author contributions:** F.W. initiated the project. F.W. and W.Z. conceived the experiments. W.Z. conducted the experiments and analyzed the data. L.W. and Y.Z. assisted with the EELS data analysis; and D.-H.S., T.C., and G.C. performed the DFT, nudged–elastic-band, and EELS simulations. M.T. and D.L. performed the spectral simulations using the OCEAN package. W.Z., D.-H.S., T.C., D.L., G.C., and F.W. wrote the paper, and all the authors were involved in revising the manuscript. **Competing interests:** The authors declare that they have no competing interests. **Data and materials availability:** All data needed to evaluate the conclusions in the paper are present in the paper and the supplementary materials. Additional data related to the computational work in this paper are available on the Materials Cloud website through the following link: https://archive.materialscloud.org/2020.0006/v1.

SUPPLEMENTARY MATERIALS

science.sciencemag.org/content/367/6481/1030/suppl/DC1
Materials and Methods
Supplementary Text
Figs. S1 to S24
References (*28*–*40*)
Movies S1 and S2

15 March 2019; accepted 30 January 2020
10.1126/science.aax3520